communications physics

A Nature Portfolio journal

Article

https://doi.org/10.1038/s42005-025-02178-y

All hard X-ray transient grating spectroscopy

Eugenio Ferrari[1,2,23] ✉, Hiroki Ueda[3,23] ✉, Danny Fainozzi[4], Taito Osaka[5], Filippo Bencivenga[6], Max Burian[7], Pietro Carrara[8,9], Joan Vila-Comamala[3], Riccardo Cucini[9], Christian David[3], Alessandro Gessini[6], Simon Gerber[3], Andrii Goloborodko[10], Ales Hrabec[11,12], Ichiro Inoue[5], Yuichi Inubushi[5,13], Ludmila M. Diniz Leroy[3,7], Riccardo Mincigrucci[6], Eugenio Paris[3], Bill Pedrini[3], Benedikt Roesner[3], Jérémy R. Rouxel[14], Carles Serrat[15], Valerio Scagnoli[11,12], Kensuke Tono[5,13], Makina Yabashi[5,13], Jumpei Yamada[5,16], Kohei Yamamoto[17,18], Marie Christine Zdora[3], Martin Beye[1,19], Claudio Masciovecchio[6], Majed Chergui[6,20], Urs Staub[3] & Cristian Svetina[3,21,22] ✉

Optical-domain transient grating (TG) spectroscopy is the ideal tool to investigate transport phenomena in gases, liquids and solids, but it is limited to typically micron-size grating periods. Extreme-Ultraviolet TG has represented a major leap forward to access the mesoscopic scales. Hard X-ray TGs open access in principle to the nanoscale. Hard X-ray TGs were recently generated using the Talbot effect and probed by optical pulses, but these hinder exploiting the advantages of the nanoscale gratings. Here, we present an all-X-ray TG study, in which few-femtosecond hard X-ray pulses are used both for excitation and probing. Our experiment was performed on an amorphous film of an FeGd alloy and on a thin silicon single crystal. The results show a manifestation of the TG induced by the X-ray pump and probe pulses in the form of Talbot carpets, as well as temporal evolution of the grating in crystalline silicon showing coherent optical phonons. Ultrafast all-X-ray TG spectroscopy has the potential to study fundamental excitations with femtosecond time resolution and nanometer spatial sensitivity.

A microscopic understanding of matter requires the study of excitations across a broad range in space, time, and frequency. The length-scale of tens of nanometers is particularly important for transport phenomena in condensed matter, as it represents the transition between diffusive and ballistic regimes. On the nanometer scale, order/disorder and static/dynamic transitions occur in charge/spin/orbital and lattice degrees-of-freedom, and relevant physical phenomena require quantum descriptions. Optical-domain four-wave mixing methods, and in particular transient grating (TG) spectroscopy, have been extensively employed for studying dynamical and transport phenomena in various materials[1]. Optical TG spectroscopies demonstrated access to all the above degrees of freedom, but are limited to typically micron-size grating periods. With the advent of Free-Electron Lasers (FEL) delivering ultrashort pulses of extreme ultraviolet (EUV) to hard X-ray photons, novel perspectives are emerging for the development of short-wavelength non-linear optics and spectroscopies[2]. In standard TG spectroscopy, two identical incident beams are crossed at the sample. An excitation grating is generated, and the evolution is monitored by a third, time-delayed probe pulse. The Leone group recently reported on near-infrared induced TGs probed by EUV pulses at a temporal resolution of attoseconds to few-fs using a HHG source[3–7]. The implementation of TG spectroscopy at FELs was first demonstrated in the EUV range[8–10], then in the hard X-ray regime[11,12]. These experiments used an optical pulse to probe the evolution of the TG generated by EUV or hard X-ray pulses. In this case, meso- to nanometer scale grating cannot be used and the advantages are lost. One needs instead to probe the TG with a third EUV or hard X-ray pulse. This requires three beams, with possible control of the time delay between the first two (pump) beams and the third (probe) beam. This was achieved in the EUV at the FERMI FEL, using a split and delay geometry allowing to generate three beams, with the third having a delay tuneable with respect to the first two[13–15]. For the soft X-ray range, an elegant scheme was recently introduced by Morillo-Candas et al. using a focused soft X-ray beam going through a spatial mask consisting of holes, such that three beams emerge, with two crossing at the sample and forming a TG, and the third probing it[16]. These developments offer new opportunities to probe dynamics but have limitations in spatial resolution, especially to probe transport phenomena when the mean free path of the excited carriers in

A full list of affiliations appears at the end of the paper. ✉e-mail: eugenio.ferrari@desy.de; hiroki.ueda@psi.ch; cristian.svetina@imdea.org

solid materials or reactants in chemical systems is shorter than the excitation grating period.

In order to generate TGs with hard X-ray beams, the so-called Talbot effect was used[17] avoiding complex optical schemes[13]. A single beam passes through a phase mask grating, leading to several diffracted beams that cross and interfere at characteristic, so-called Talbot distances. An interference pattern is then formed that is termed "Talbot carpet". The "carpet period" is determined by the wavelength of the incident radiation, the pitch of the mask and the convergence/divergence of the beam[11,12]. Here we demonstrate all hard X-ray TG spectroscopy on a test sample consisting of a film of FeGd and on the main sample, consisting of a thin silicon single crystal. Both are prototypical samples for all-optical switching devices and semiconductor technology.

Results and discussion

An all hard X-ray TG experiment requires two pulses with controllable photon energy, intensity, and relative time delay. Here, we take advantage of the versatility of the SACLA XFEL source (Hyogo, Japan)[18], which delivers two collinear ultrashort hard X-ray pulses (~7 fs temporal width each), at photon energies of 5 keV and 7.24 keV and variable time delays between 2 and 300 fs. The probe beam was tuned to the Gd L_3 edge to maximize the response from the FeGd film. Adjusting the delay between the accelerator-generated X-ray pump and probe beams necessitates precise and sophisticated control of the electron beam dynamics[19]. Furthermore, both pulses can each create a Talbot carpet after going through the phase mask, though with different Talbot distances. Aluminum and vanadium solid-state filters were employed to regulate and fine-tune the relative intensities of the two pulses at the sample.

The experimental layout is shown in Fig. 1. The slightly convergent 5 keV pump pulses pass through the gold phase mask. The latter has a grating pitch of 200 nm, and is placed at a distance to the sample that can be scanned between 3.5 and 8 mm (see "Methods"). In this geometry, the TG pitch at the sample is slightly reduced with respect to the mask's pitch and is estimated to ~194 nm. Two detectors are used to monitor the signal: (1) an X-ray MultiPort Charge-Coupled Device (MPCCD) camera[20] positioned in transmission for the signal diffracted by the transient grating (thereafter called transmission detection); (2) a MPCCD detector positioned at the Si(222) Bragg angle in the horizontal plane, to study the TG response on the Bragg diffraction peak (thereafter called diffraction detection). Silicon crystallizes in a diamond structure, characterized by two interpenetrating face-centered-cubic (fcc) sub-lattices displaced by a quarter of the distance along the cube diagonal. Each unit cell contains two atomic positions, with the atoms having a tetrahedral site symmetry, and being related by inversion symmetry. When the two atoms are perfectly identical, the (222) reflection is forbidden. However, the distribution of scattering matter in diamond-like crystal structure may not be centrosymmetric, as any perturbation of the atoms reflecting their tetrahedral site symmetry will contribute a non-centrosymmetric component to the distribution of scattering matter, and thus yield a non-zero (222) reflection. Examples of such perturbations are the tetrahedral orientation of the covalent bonds in these crystals, and the anharmonicity of the interatomic potential[21]. This makes the detection of the Si(222) reflection exciting due to its inherent electronic character and its ability to reveal lattice anharmonicities. In the present study of crystalline silicon, we employed various filter settings to generate three regimes of the incoming beam intensities that correspond to different ratios ($R = I_{pump}/I_{probe}$) of the pump and probe intensities. For the amorphous FeGd sample,

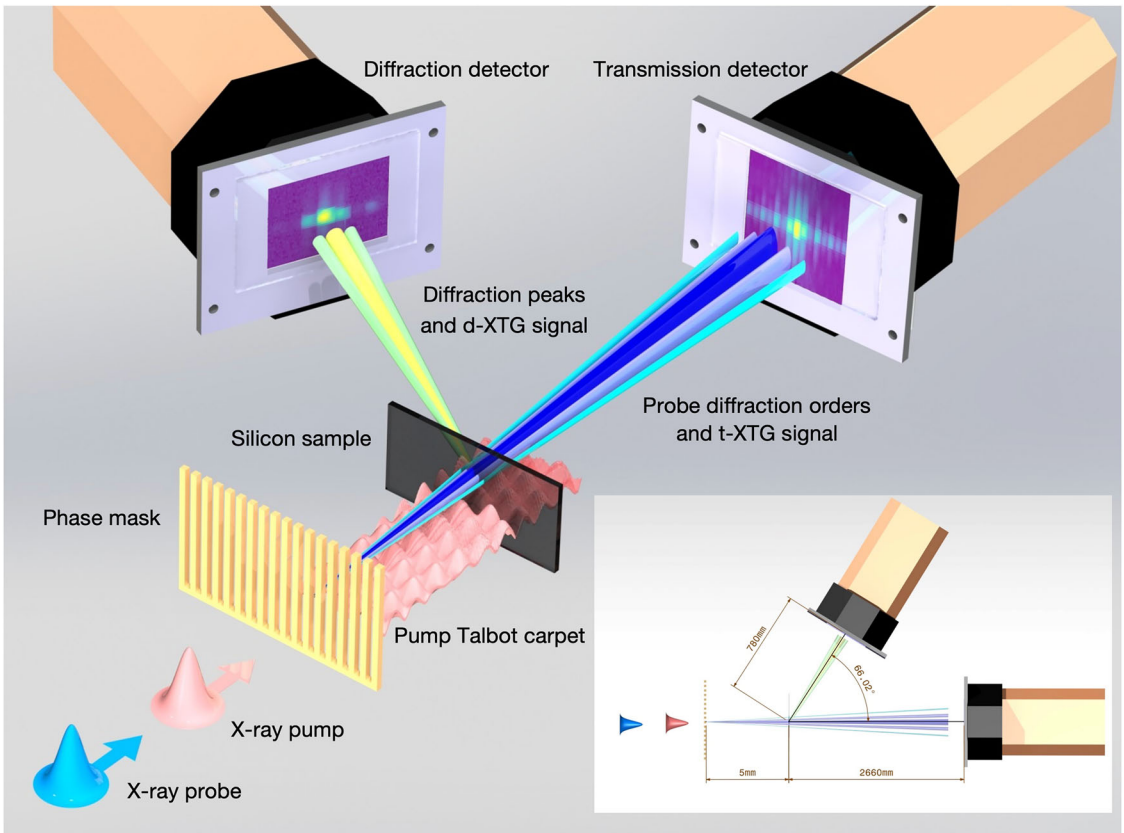

Fig. 1 | Experimental geometry of the All X-ray Transient Grating experiment. Perspective scheme of the experimental setup: both collinear pump (pink) and probe (blue) X-ray beams pass through the phase mask. The sample is placed in the Fresnel zone (several Talbot distances of the pump), thus generating therein an excitation interference pattern, while the probe beam is detected in transmission (right detector) and diffraction (left detector) geometry. Several diffracted beams emerge from the mask and undergo diffraction onto the lattice and the TG. Inset: sketch of the experimental set-up (top-view) with relevant distances and angles.

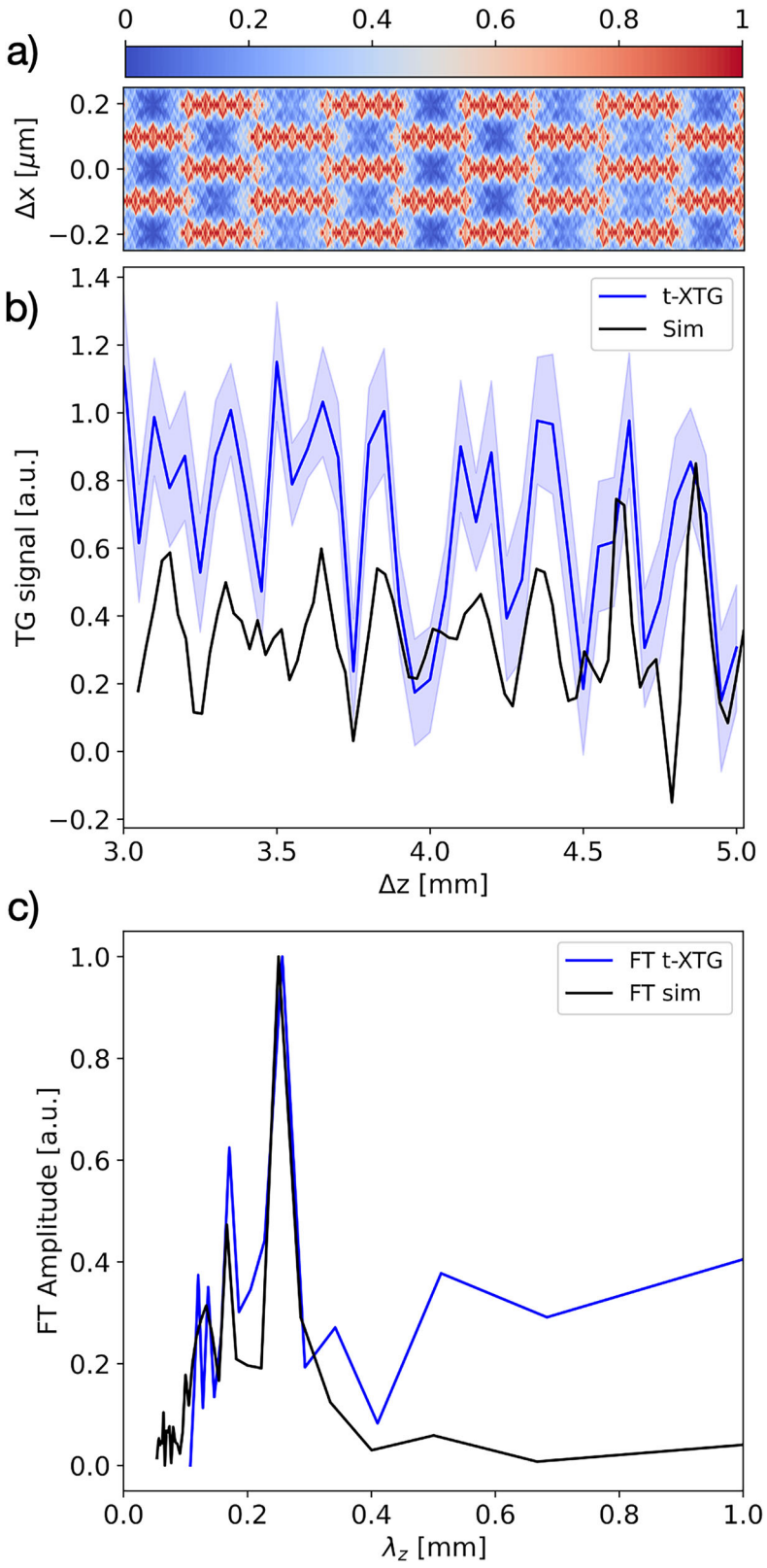

Fig. 2 | Comparison between experimental data and simulations of the Talbot carpet from FeGd. **a** Simulated Talbot carpet matching the experimental conditions. **b** All hard X-ray transient grating signal (blue) of a FeGd thin membrane, as a function of the mask-sample distance. The sample goes through several Talbot planes (simulated Talbot carpet in the upper panel, in arb. u.), each causing a maximum signal. The blue shaded area represents the signal including the standard deviation. Wave-front propagation simulation (black trace, vertically shifted for clarity, see "Methods" for details) reproduces this trend. The simulated trace has been normalized to 1 but it actually displays modulation up to 20%. **c** Fourier transform of the experimental and simulated traces of the distance scan, showing main peaks at 175 μm and 255 μm periodicity of the Talbot carpet, corresponding to the values for the pump and probe beams, respectively. In both the experiment and the simulation, the ratio of pump to probe intensities is 0.1.

the X-ray probe beam was detected in transmission through the sample only.

To find clear signatures of TG signals, the phase-mask—sample distance is varied for both samples: in this way, the Talbot carpets move through the sample with consequent modulation of the excitation which, in turn, critically affects the nonlinear TG signal whose intensity will resemble the excitation pattern. This is shown in Fig. 2, where the evolution of the transmission signal as a function of mask-sample distance is displayed for a thin FeGd film (1.7 μm thick), at a fixed pump-probe time delay of 200 fs. A marked modulation (~20%, well above the noise level) of the transmitted beam intensity is observed. To determine the origin of the modulation, we present a simulated sample irradiance that accounts for the effects of both pump and probe intensities on the sample illumination. This illumination can be represented as a Talbot carpet, formed by both pump and

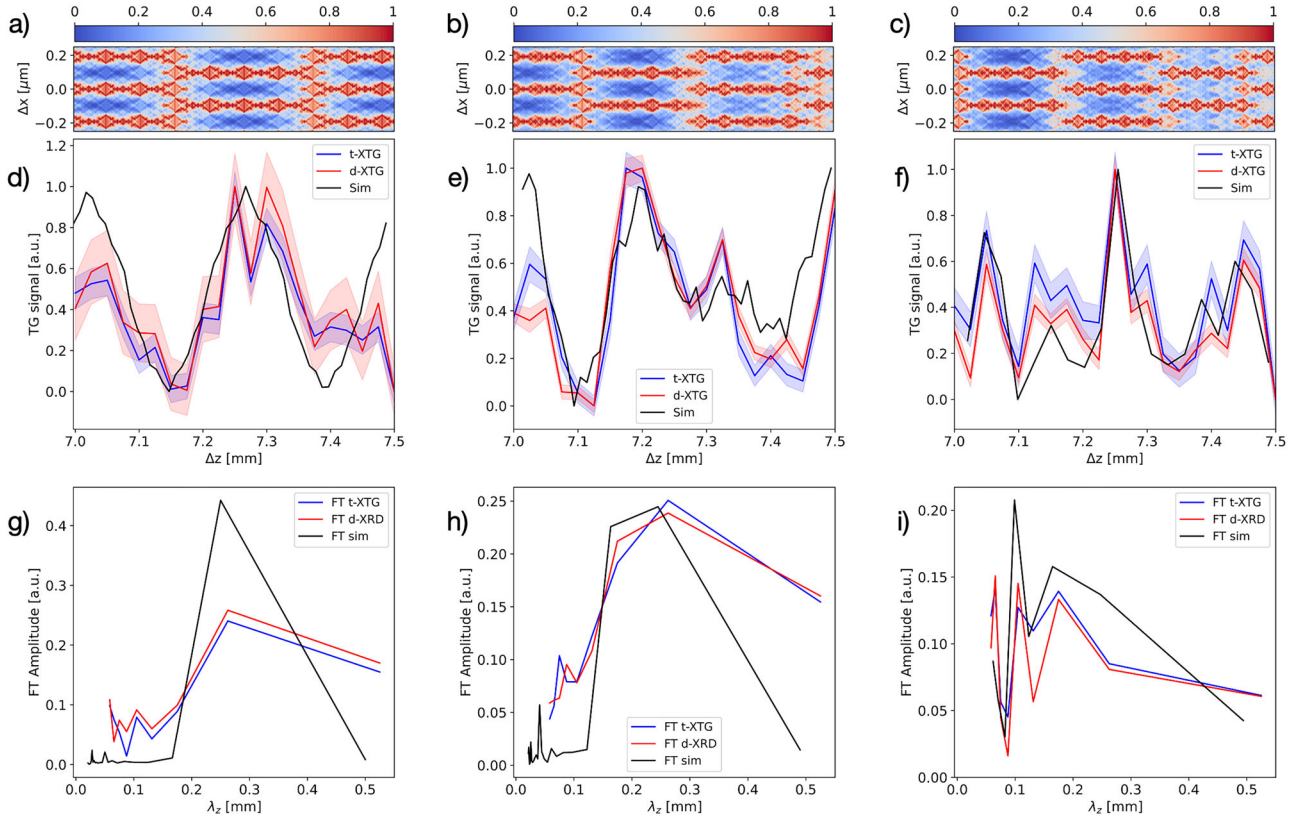

Fig. 3 | Comparison between experimental data and simulations of the Talbot carpet from Silicon at different pump/probe intensity ratios. d–f All hard X-ray transient grating signal of crystalline silicon as a function of the distance between the phase mask and the sample using 25 μm steps over a 500 μm scan range and related FT (**g–i**). Both the diffraction (red) and transmission (blue) signals are detected for: **a** weak pump pulse (2.5×10^{-4} μJ) at 2 fs time delay, intense probe pulse; **b** pump and probe pulses of comparable intensities (0.4 μJ) at 2 fs time delay; **c** intense pump pulse (1.9 μJ) and weak probe pulse at 10 fs time delay. The red/blue shaded areas in (**d–f**) represent the signal, including the standard deviation. The (**a–c**) panels are the real space representation of the Talbot carpets (in arb. u.) as a function of the distance (Δz) between the phase mask and the sample. The theoretical traces (black) reproduce the spatial modulation generated by the pump- and probe-induced Talbot carpets with periods of 175 μm and 255 μm, respectively. The traces have been normalized to 1.

probe intensities, including their ratio (Fig. 2a; see "Methods" for details). Figure 2b compares the normalized experimental and simulated traces obtained from the simulated far-field one-dimensional patterns by integrating across the lateral size Δx, considering only diffraction orders from −1 to +1. There is a direct correspondence of the structures in the measured signal (blue) and the complex simulated pattern (black). The Fourier Transform (FT) of both experimental and simulated traces are shown in Fig. 2c: the far-field TG signal exhibits the expected modulation generated by the pump beam at 5 keV with a periodicity of 175 μm. This confirms that the X-ray probe beam indeed detects the X-ray pump-induced TG. A sufficiently intense beam can also generate a TG from which it can diffract in what is called self-diffraction[16]. In case the second pulse (the probe) has enough intensity, it will self-diffract and its signal will appear showing the characteristic period given by its photon energy. The FT in Fig. 2c exhibits a second, dominant periodicity appearing at a distance of 255 μm, which corresponds to the distance of the Talbot planes for the probe beam at 7.24 keV, identified as the self-diffraction. We also identify the presence of pump- and probe-induced TG harmonics at Talbot distances of 350 μm and 510 μm, respectively, though at the sampling limit.

In non-collinear geometries, the TG signal is background-free[22]. The collinear geometry used in the present work generates multiple signal beams, which do not allow for a background-free detection. Nevertheless, it offers at the same time detection of higher diffraction orders that provide additional insights into the dynamical properties of the sample[23]. While in the present experiment, we were constrained to the collinear geometry, our results point to a clear path for future developments, and the use of dedicated split-and-delay lines[13] will allow for more complex geometries.

We now turn to the results on the silicon sample (10 μm-thick, orientation <100>). Figure 3 shows the simulated sample irradiance (a–c) and the corresponding sample scans (d–f) and FTs (g-i) detected both in transmission (blue) and diffraction (red) geometries for different intensity ratios R of the pump and probe pulses: (a) $R = 0.06$, i.e., the probe self-diffraction is dominant and the pump is very weak (2.5×10^{-4} μJ); (b) $R = 0.9$, i.e., the pump and probe have comparable intensities (pump intensity = 0.4 μJ), and; (c) $R = 6$, the high-intensity pump and low-intensity probe (pump intensity is 1.9 μJ).

The data shows a good correspondence between the diffraction and transmission signal detection channels for all three cases. Here again, the observed structures in the signal are complex, but clearly above the noise level, and they compare well to the simulated traces (black). Already a visual inspection reveals the main features, similar to the case of FeGd: (i) with a weak pump beam (Fig. 3a, d, g), an oscillation period around 255 μm reflects the self-diffraction of the probe beam; (ii) with comparable pump and probe intensities (Fig. 3b, e, h) an additional oscillation emerges at ~175 μm period generated by the pump pulse; (iii) the latter is the remaining periodicity when the probe beam is attenuated (Fig. 3c, f, i).

The attenuated probe beam condition is then used to perform a pump-probe time delay scan by tuning the accelerator (see Fig. 4). As a check of systematic but undesired signal contributions, a scan is performed without the sample, and shown in Fig. 4a. A peak appears at early times, around 15–20 fs, followed by a subsequent rise of the signal beyond 50 fs. This is interpreted as a response of the diffraction efficiency of the gold phase mask to the pulse sequence. Prior to discussing this effect in more detail, we introduce Fig. 4b, which shows the diffraction (red) and transmission (blue)

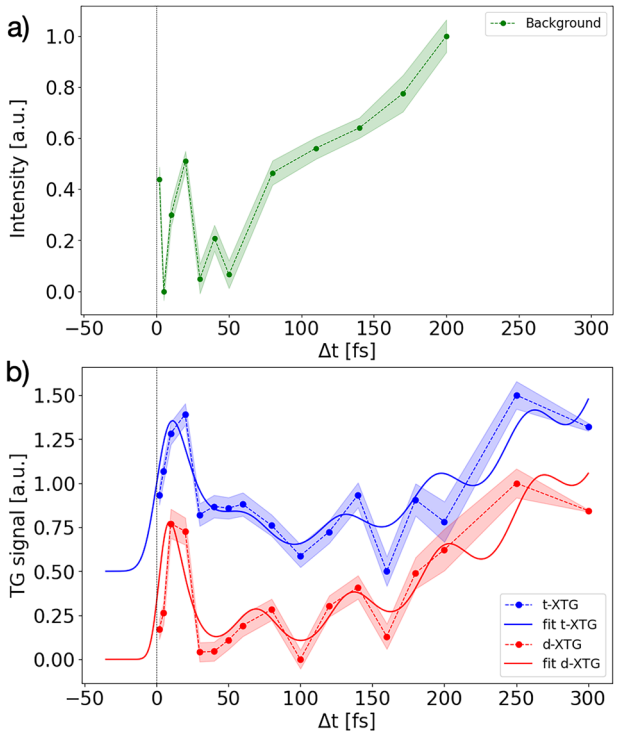

Fig. 4 | Comparison between time scans without and with silicon sample. a Time-scan of the pump-probe delay without sample. The trace shows non-monotonic dynamics at early times attributed to the ultrafast response of the phase mask irradiated by the pump beam before diffracting the probe beam. At longer time delays the probe intensity increases, and no oscillation is detected. **b** Time-scan comparison of the diffraction (red) and transmission (blue) signals of crystalline silicon, showing a coherent oscillation of 16 ± 0.7 THz matching the Si optical phonon with frequency around 15.5 THz. The red/blue shaded area represents the signal including the standard deviation. The fits (lines) of the experimental traces are a guide to the eye and were performed using the TG equation and a linear term to follow the rise of the probe intensity (see text). The procedure and analysis used to extract the data points is described in the "Methods" Section.

signal traces of the silicon sample. Both independent detection modalities show a correspondence, characterized by a very fast (<10 fs) rise, reaching a maximum at ~15–20 fs delay, and additional maxima appear around 75–80 fs and 130–140 fs. A rising background shows up beyond ~150 fs. Unfortunately, a quantitative comparison between the scan with and without a sample is difficult, since different experimental conditions had to be used. Nevertheless, similarities between the two scans are limited to the peak at earliest times. Since the data shown in Fig. 3 has been obtained at fixed pump-probe delay at such early times, by scanning the sample position, this peak must also contain a significant sample response. We also note that the increase in background with delay seems to occur at later times when the sample is present. Larger time delays were not possible with the actual accelerator set-up. Most important, the scan with the sample (Fig. 4b) exhibits modulations, absent without sample, whose period aligns with the frequency of the single triply-degenerate optical phonon mode at the zone center of silicon (~65 fs or ~15.5 THz) as reported in frequency-domain Raman spectroscopy[24] and time-domain experiments[25,26]. This points to the generation of coherent optical phonons in our experiment, which we discuss below. Therefore, although we can at this stage not subtract the scan without the sample from the scan with the sample, characteristic features appear which pertain to the physics of the sample. Below, we also argue why the initial peak, which appears in both scans, may indeed be present with and without a sample.

A model represented by the typical TG equation plus a linear term that takes into account the rise at longer time delays (as detected in the trace without sample) was used to generate the continuous trace in Fig. 4b, to reproduce the diffracted and transmitted signal traces[27]:

$$I_{TG} = \left| c_1 \left[\frac{1}{2} + \mathrm{erf}\left(\frac{\Delta t}{\sigma} \right) \right] \times \left[c_2 e^{-\frac{\Delta t}{\tau_1}} + c_3 \cos\left(2\pi\nu\Delta t + \phi\right) e^{-\frac{\Delta t}{\tau_2}} + (m\Delta t + q) \right] \right|^2$$

The error function is used to model the sharp rise often fixed by the time resolution. The exponential decay term, usually used to model the thermal decay of the TG signal, is used here to reflect a fast electronic decay and is followed by a damped oscillatory term representing the Si optical phonon at our transferred momentum. The linear term empirically models the response of the phase mask alone, here considered as background, and represented by the "m" and "q" values which do not carry additional physical meaning. This term thus represents the background rise and is necessary to provide a proper guide-to-the-eye for the reader otherwise the fit cannot follow this rise. In the equation, $\Delta t = t\text{-}t_0$ is the time delay, σ is the width representing the time resolution, c_1, c_2 and c_3 are intensity constants, τ_1 is the electronic decay time, τ_2 is the phonon decay-time with frequency ν (16 THz) and phase shift ϕ (2.6 rad). The good agreement between the experimental and simulated traces shows that the data is consistent with diffraction from coherent optical phonons with a momentum induced by the TG period (in case of the (222) reflection, the momenta of the reflection and the TG are combined).

The generation of coherent phonons by short-wavelength pulses is quite surprising in itself. The mechanism remains unclear, despite the frequent observation of coherent optical and acoustic phonon generation in EUV[9,13] and hard X-ray[12] TG experiments on solid materials, while Huang et al. reported coherent acoustic phonons in an all hard X-ray pump-probe scattering experiment on bulk $SrTiO_3$ and $KTaO_3$ single crystals[28]. In the case of Bismuth Germanate ($Bi_4Ge_3O_{12}$, denoted as BGO), the 2.7 THz (370 fs) optical phonon was observed by optical impulsive stimulated Raman scattering (ISRS)[29,30], in EUV-TG experiments using 12.7 nm pump pulses and an optical probe[9], and in hard X-ray experiments using 7.1 keV pump pulses and an optical probe[12]. Likewise, the 65 fs phonon of crystalline Si in the present study has been reported in optical-domain ultrafast transient reflectivity[31,32], impulsive stimulated Raman[25], and in transient electro-optic measurements[26]. Depending on the excitation conditions, the generation process was found to have a displacive (cosine dependence) or a non-resonant impulsive stimulated Raman scattering (ISRS, sine dependence) origin, although intermediate situations may arise[25,33]. The observations on BGO and the present ones on crystalline Si show that the generation of the coherent phonons is independent of the excitation energy. While this does not exclude the ISRS mechanism in the case of the optical excitation, it is ruled out in the case of EUV or hard X-ray excitation and we believe that the observed coherent optical phonons are driven by the electronic excitation via the displacive mechanism. In the work by Huang et al., the generation of coherent acoustic phonons was related to the photoelectron and Auger electron cascade dynamics, as well as the electron-phonon interaction[28].

The origin of the first peak at 15–20 fs in Fig. 4 deserves examination. It occurs even in the absence of the sample. While a definitive assessment of its origin is not possible at this stage, we believe that the pump pulse may induce an ultrafast electronic response in the phase mask. Indeed, with 5 keV photon energy in the pump pulse, the M-shells of Au are most likely excited. Such an excitation will decay on the scale of the core-hole lifetime of <4 fs[34], and generate an electronic cloud from additional, sub-fs intra-atomic decay channels. Indeed, calculations[35] have shown that 8 keV/10 fs XFEL pulses at a fluence of 5×10^{12} photons/μm^2 can strip 20 electrons from Fe atoms within 10 fs. The temporal dynamics of such an electronic cloud around the atoms in the phase mask will alter the diffraction properties of the mask and yield the appearance of the first peak in the signal. As alluded to above, it is likely that the crystalline Si sample may also contribute to the first temporal peak, and for the same reasons as invoked in the case of the gold mask. And indeed, its delayed appearance would be caused by the same electronic response as in the case of the gold mask. In addition, we note that it does fit nicely in the sequence of oscillations due to the 65 fs mode. Should this

hypothesis be confirmed, we have evidence of the temporal evolution of hot photo- and Auger electrons preceding the generation of coherent optical phonons.

Conclusions

In this work, we demonstrated all hard X-ray transient grating spectroscopy, where both the pump and probe beams operate in the hard X-ray regime, on two samples: films of amorphous FeGd and crystalline silicon. In the latter case, the X-ray TG response was monitored both in transmission and using X-ray diffraction. This ability to combine the two detections offers additional insight, since the detected momentum transfer (Q) range can vary significantly between the transmission and diffraction geometry. Indeed, the Q-range in transmission is due to the inverse of the grating period, while in diffraction, it is the sum of the Q-vectors due to Bragg reflection and due to the TG. For the proof-of-concept and the observation of TG signals induced and probed by hard X-rays in the first place, the present work utilized TG grating periods that are significantly larger than those ultimately achievable with hard X-rays. This is a consequence of the chosen geometry but the implementation of phase masks with smaller pitch or an X-ray set-up based on crystal reflection has the potential to reach sub-nm TG periods[36].

The time-resolved trace on the phase mask shows an early time-response which we attribute to electron dynamics whose complete interpretation requires additional studies. Such dynamics act as a modulation of the probe beam at the sample for which, unlike for the time-independent spatial scans, a simple normalization with respect to the intensity from the source is not enough. Unfortunately, the traces were acquired in different experimental conditions and a normalization accounting for the phase mask's temporal response was not possible. We underline that this limitation is not due to the TG method that, like every spectroscopic technique, requires normalizations. Indeed, a proper acquisition of a reference trace without sample would immediately solve this problem. Another more complex alternative requires the pump beam to pass through the phase mask to generate the Talbot effect while the probe beam does not pass through the mask. This would not modulate the probe beam intensity at different time delays but would require a non-collinear geometry which, in turn, needs the implementation of additional optics such as split-delay lines and grazing incidence mirrors. Even without normalization for the trace without sample, the main result on crystalline silicon is the appearance of a coherent optical phonon, not present in the phase mask trace. The mechanism behind the generation of coherent phonons still needs to be clarified, as well as the origin of the surprisingly strong signals.

We also demonstrated self-diffraction in the hard X-ray regime. This opens the fascinating possibility of TG experiments using a single pulse, with the excitation occurring in the leading edge of the pulse while the probing occurs in its trailing edge. Given the very short pulse durations used here (~7 fs), this allows for the investigation of phenomena taking place within the pulse duration, i.e., within a few femtoseconds or less. Combining this time resolution with spectroscopic tuning through core resonances could provide an exciting and elegant approach for investigating electronic dynamics that precede structural changes. The scheme used in the present paper is reminiscent of a similar one implemented in the optical domain by Katayama et al.[37], in which they used heterodyne detection. This is a promising avenue for the present work.

Our study identifies key factors that could unlock previously inaccessible spatial—and thus momentum—regions, potentially advancing the TG approach for nanoscale dynamics in condensed matter systems. This high-sensitivity technique enables low-fluence experiments, addressing the challenge of high-intensity irradiation in FEL-based material studies. Understanding nanoscale dynamics is key to developing next-generation materials, including miniaturized thermal devices, superconductors, and ultrafast data storage. In particular, nanoscale thermal transport studies are vital for improving heat management in micro- and nano-electronic devices.

Moreover, all X-ray TG emerges as a complementary technique to inelastic neutron[38] and X-ray[39] scattering, which are widely used to study collective dynamics in condensed matter. However, these scattering methods face significant limitations when probing nanoscale phonon modes, especially in disordered systems such as liquids or glasses, where the absence of periodicity necessitates the study of phonon-like modes in the first pseudo-Brillouin zone[39].

The attosecond time-resolution achievable in the EUV is becoming available in the hard X-ray range[40], opening the possibility to investigate resonant core-hole induced dynamics before thermalization by all hard X-ray TG, and with element-selectivity in both the excitation and the probing steps. A promising avenue of attosecond hard X-ray TG is the use of two broadband pulses for excitation and one for probing, which could span more than one core transition and allow detecting cross-talk between atomic centers in a molecule or a solid. This would be the route towards multi-dimensional X-ray spectroscopies.

This first demonstration of all hard X-ray TG spectroscopy calls for further experiments at XFEL facilities, which will address the numerous open questions raised by the present work.

Methods

Beamline and instrumentation

The experiment was performed at beamline BL3 (EH4c) of the SACLA Free Electron Laser (Hyogo, Japan)[41]. Two collinear X-ray pulses were generated from the same electron bunch in two undulator sections with variable undulator parameters. In the first undulator section the pump pulses at 5 keV were emitted with intensities up to 100 μJ, and in the following section, the probe pulses at 7.24 keV with intensities up to 50 μJ. Time delays between the two pulses ranging from 2 fs up to 300 fs were provided by controlling the electron bunch pathway through a magnetic chicane located between the two sections[19]. The focusing was provided by a set of total-reflection elliptic mirrors arranged in the Kirkpatrick-Baez (KB) geometry with a focal length of 1300 mm in the diffraction plane of the phase mask (horizontal)[42]. Upstream the KB mirrors, an online spectrometer that consists of a 15-μm-thick nanocrystalline diamond film and a 2-dimensional detector[43] was installed to measure single-shot spectra and relative intensities of the two pulses. Spatial content of the X-ray beams outside the aperture of the KB mirrors was rejected by 4-jaw slits located in front of both the online spectrometer and the KB mirrors. The phase mask generating the Talbot carpet was made of gold with a pitch of 200 nm, duty factor 0.5 and a phase shift of $\pi/2$ at 5 keV[44]. The test sample used for the long spatial scan (Fig. 2) was a thin film of FeGd (thickness 1.7 μm) deposited on a silicon nitride membrane. The main sample was a 10 μm-thick silicon single crystal in <100> orientation. The phase mask and the sample were mounted in air on translation/rotation stages allowing for fine alignment. The average distance between phase mask and sample was about 5 mm. Transmission and diffraction signals were measured by multi-port charge coupled devices (MPCCDs)[20] placed, respectively, 2660 mm and 780 mm downstream the sample. Pump and probe beam sizes at the sample were measured before the experiment with a knife-edge scan method showing 100 μm × 65 μm and 55 μm × 55 μm Full Width at Half Maximum (FWHM) for the pump and probe beams, respectively.

The X-ray diffraction (XRD) detector was placed in the horizonal scattering plane to collect the (222) forbidden-peak of silicon with close to normal incidence (89.4°) to the (100) surface in Laue geometry, having $\delta \approx 0°$ (horizontal scattering), $\gamma = 66.2°$, $\omega = -133.9°$ ($\omega = 0$ having (01-1) axis horizontal). Aluminum and vanadium solid state filters of different thicknesses (the vanadium foil was 25 μm-thick, while the aluminum was varied between 18 and 168 μm) were used before the phase mask to attenuate and control the intensity of both pump and probe beams while a thick (168 μm) aluminum foil was placed in front of the MPCCD in transmission to avoid contamination of the pump beam on the detector. The geometry of the experiment is sketched in Fig. 1 (inset, not to scale).

Data treatment and nonlinearity of the signals

The single shot spectra for pump and probe pulses were measured on a dedicated on-line spectrometer based on a bent silicon crystal and a 2-dimensional X-ray detector. Both spectra were fit to a double Lorentzian

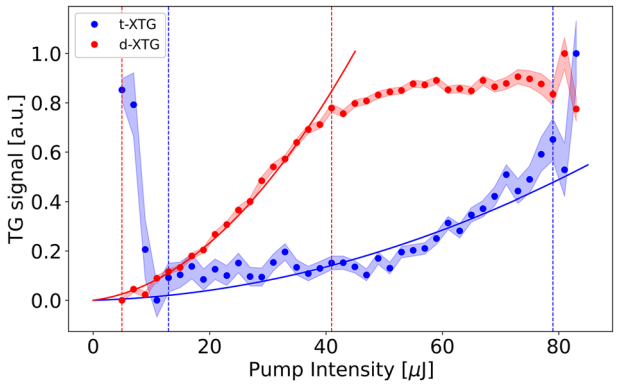

Fig. 5 | Nonlinearity of the transient grating signal as a function of the pump intensity. All X-ray TG signal intensity in transmission (blue) and diffraction (red) at $Z = 7.3$ mm and $t = 2$ fs as a function of the pump intensity. The shaded areas for each trace correspond to the signal including the standard deviation. Areas included in the vertical red/blue dashed lines represent the minimum and maximum intensities considered in the analysis of the quadratic behavior of the d/t-XTG signals. The blue trace shows outliers for low (below 10 μJ) and high (above 80 μJ) pump intensities (at the source), while the red trace shows a plateau at high pump intensities (above 40 μJ). This behavior is probably due to saturation of electron delocalization effects for high incident beam intensities. This effect does not affect the transmitted TG signal.

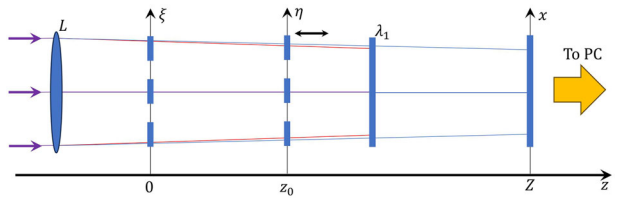

Fig. 6 | Schematic diagram of an optical set-up for far-field intensity distribution measurements. Two divergent beams (pump in blue and probe in red) illuminate from the left the phase mask situated in the plane $z = 0$, positioned after the lens (L). Each beam has its own radius of curvature which causes different beam radius at the phase mask plane. Due to the Talbot effect, transient grating excitation is formed on the sample (placed at a distance z_0 from the phase mask). The far-field diffraction pattern is recorded by a two-dimensional position-sensitive detector, which is situated on the distance Z from the phase mask. The coordinate system is the following: ξ represents the in-plane coordinate of the grating ($z = 0$), η denotes the coordinate at the sample plane ($z = z_0$), and x is the coordinate at the plane of the position-sensitive detector ($z = Z$).

curve to assign individual intensities for both X-ray pulses, also taking into consideration the transmission of the beamline at the two different photon energies. Spatial and time scans were performed with 2000 to 4000 shots per step and the intensities (2D images) were collected by the MPCCD detectors on a shot-to-shot basis. Each 2D image was normalized by the probe intensity on a shot-to-shot basis filtered for outliers such as: pump/probe intensities below/above 10/80 μJ and 1/40 μJ respectively, and pump/probe energy spectra peak position and bandwidth (i.e., ensuring spectral purity and stability of both pulses). Whenever possible, intensity scans of the pump pulse were acquired taking advantage of the natural SASE fluctuations in pulse energy.

Due to the geometry of the experiment, different regions of the detector showed the presence of the TG signal due to multiple diffracted beams overlapping at specific regions of the detector. The intensity pattern at the detector in transmission shows a series of diffraction peaks in the horizontal plane (displayed in Fig. 1): the probe beam is diffracted by the phase mask into several probe beams passing through the sample and reaching the detector. The pump beam excites the sample and the transmitted part is absorbed by solid state filters in front of the detector. Each probe beam reaches a region illuminated by the TG and generates a signal beam that, given the experimental collinear-geometry, overlaps with a diffraction order. The centroid of these signal beams is slightly shifted with respect to the diffraction beams due to the fact that the periodicity of the TG at the sample was slightly demagnified, i.e., about 194 nm instead of 200 nm. It can be seen that for the presented case, the angular separation between transmitted probes and signals is negligible (few tens of microrads for the first order of diffraction and a consequent spatial separation less than 70 μm). Considering that the spot size of the probe beams at the detector was about 2.5 mm, it was not possible to detect background-free signals in this geometry. This problem can be solved in the future by adopting a non-collinear geometry that, however, requires the use of additional X-ray optics and a higher level of complexity. Nevertheless, after normalizations and filtering, as described above, we were able to detect the signals presented in the main text, displaying the expected fingerprints of the Talbot carpets as well as nonlinear behaviors.

A similar argument applies for the intensity pattern on the detector in diffraction (also shown in Fig. 1) which displays a main Bragg peak (corresponding to the (222) silicon peak) and side peaks generated by the diffraction orders of the probe beam reaching the sample with a small angular mismatch due to the presence of the phase mask. Also signals were found inside these peaks because the pitch at the sample was still quite coarse and the expected side-bands related to the TG signal were inside these peaks.

In the data analysis, the regions with the highest intensity and best signal-to-noise ratio around the diffraction peaks were selected. The signal was obtained by integrating over the 2D images of the detector within these regions, after carefully removing outliers identified as the points outside the vertical dotted lines in Fig. 5, i.e., below 10 μJ and about 80 μJ for pump and above 40 μJ for the probe. The transmission TG trace shows a quadratic trend as a function of the pump energy, except for few points at the lowest intensities that are considered outliers. The diffracted TG trace also exhibits a quadratic behavior as expected, until it reaches a plateau, which we assume might be due to dynamical diffraction effects generated by the intense pump beam. It is worth noting that all the reported signals vary strongly by as much as 15–20%. This result is unexpected considering the non-resonant photon energy employed for the probe, and it calls for further investigation. Nevertheless, the reproducibility of the data and the agreement with theory are convincing evidence of the non-linear nature of the signals.

Simulations

Figure. 6 illustrates the general principles of the far-field behavior in the experiment. The input field consists of two optical beams with different wavelengths, λ_0 (pump) and λ_1 (probe), which pass through a focusing element, L. In this case, L corresponds to the KB mirrors, forming a convergent wavefront at the phase mask plane ($z = 0$).

The field scattered from the phase mask forms a grating on the sample, which is positioned at a distance $z = z_0$ from the mask. Since the sample is mounted on a movable platform, the properties of the grating strongly depend on the value of z_0. The far-field image is captured by a sensor located at a distance $z = Z - z_0$ from the sample, where a filter isolates the probe beam (λ_1) under analysis while removing the pump beam (λ_0). It is important to note that the scheme depicted in Fig. 6 is a general conceptual diagram, and the distances z_0 and Z shown do not correspond to the actual experimental scales. Throughout this discussion, we define the transverse spatial coordinate ξ in the grating plane ($z = 0$), η as the coordinate in the grating on the sample plane ($z = z_0$), and x as the coordinate in the image plane ($z = Z > z_0$).

Suppose that the one-dimensional (1D) grating transmission function can be expressed as a Fourier series:

$$T(\xi) = \sum_n C_n e^{j\frac{2\pi}{D}n\xi}, \quad (1)$$

where D is the grating period, and $\{C_n\}$ are the Fourier coefficients associated with the grating unit cell. For a Gaussian field with a waist value w, the 1D

field intensity at any distance from the grating can be expressed as[45]:

$$I_\lambda(x|z) \sim e^{-\frac{x^2(R-z)^2}{w^2R^2}} \sum_{m,n} C_m C_n^* e^{-2\left(n^2+m^2\right)\frac{D^2}{w^2}-j\pi\left(m^2-n^2\right)\frac{\lambda z}{D^2}} \times e^{\frac{x(R-z)}{R}\left(\frac{2D}{w^2}(m+n)+j\frac{2\pi}{D}(m-n)\right)} \quad (2)$$

where the symbol * denotes complex conjugation, and R is the wavefront curvature on the grating for the incident beam, which also depends on the initial curvature of the Hermite-Gaussian beam, R_0:

$$E(\xi|0) = E_0 e^{-\frac{\xi^2}{2w^2}} e^{j\frac{2\pi\xi}{\lambda R_0}}, \quad (3)$$

where E_0 represents the initial amplitude. Here and in what follows, we assume that the initial curvature of the Hermite-Gaussian beam is $R_0 = \infty$.

We now introduce the phase effectivity parameter β, which serves as a single, experimentally relevant parameter that combines material properties, beam intensities, and sample geometry to describe nonlinear phase modulation. The parameter β quantifies the nonlinear phase shift induced by the Kerr effect, integrating key material and experimental factors. It depends on the sample's nonlinear refractive index n_2, thickness, probe wavelength λ_1, and total beam peak intensity $I_0 = I_{0\lambda 0} + I_{0\lambda 1}$, determining the modulation depth of the transmitted wavefront. While β remains valid for low-loss materials, it may require corrections in high-intensity regimes where nonlinear absorption effects become significant. Assuming that such an intensity distribution creates a grating on the sample, the phase effectivity

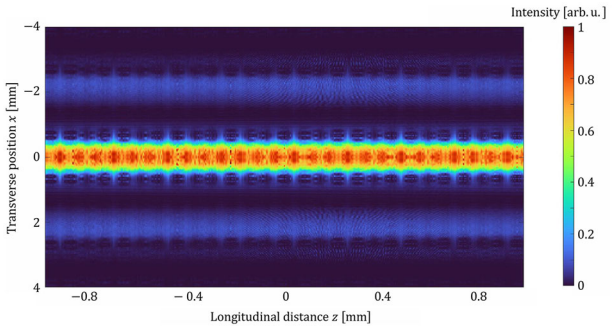

Fig. 7 | Simulated far-field image intensity distribution for different distances between grating and sample (dynamic grating). Simulation parameters are: the central distance between grating and sample is 10 mm (zero value in the figure); grating period $D = 200$ nm; phase depth of grating is 0.5 π for wavelength 0.248 nm (5 keV) and 0.3π for 0.171 nm (7.24 keV); beam waist value is $w = 97$ μm; phase effectivity parameter $\beta = 0.1$; and pump to probe intensity ratio is $p = 1$.

β appears in the transmission function as:

$$T_D(\eta|z_0) = e^{j\beta \mathrm{I}(\eta|z_0)/I_0}, \quad (4)$$

where $I(\eta|z_0) = I_{\lambda 0}(\eta|z_0) + I_{\lambda 1}(\eta|z_0)$ is the total light intensity on the sample. At any distance z from the grating on the sample, the amplitude distribution of the optical field is given by:

$$E(x|Z) = \int_{-\infty}^{+\infty} E(\eta|z_0) T(\eta|z_0) PSF(x-\eta|Z) d\eta, \quad (5)$$

where PSF(x - $\eta\,|\,Z$) represents the one-dimensional (1D) Fresnel approximation of the free-space point spread function:

$$PSF(x-\eta|Z) = \frac{1}{\sqrt{j\lambda Z}} e^{j\pi\frac{Z}{\lambda}} e^{j\pi\frac{(x-\eta)^2}{\lambda Z}} \quad (6)$$

One can now observe that Eq. (5) can be rewritten as:

$$E(x|Z) \sim \sum_n C_n \int_{-\infty}^{+\infty} \int_{-\infty}^{+\infty} E(\xi|0) e^{j\frac{2\pi}{D}\eta\xi} T(\eta|z_0) e^{j\pi\frac{Z(\xi-\eta)^2+z_0(x-\eta)^2}{\lambda Z_0}} d\xi d\eta. \quad (7)$$

Since Eq. (7) cannot be solved analytically, computer simulations are performed. The grating on the sample, T_D, expands the spatial spectrum of the far-field image, leading to the appearance of additional diffraction orders. It is important to note that there exists a specific distance, denoted as Z_{max}, beyond which the different diffraction orders no longer interfere with each other:

$$Z_{\max} = Z_T \frac{w}{D}\left(1 - \frac{Z_T}{R}\right)^{-1}, \quad (8)$$

This distance can be easily determined using geometrical analysis. For any distance greater than Z_{max}, the Talbot planes disappear, indicating a transition from the Fresnel regime to the Fraunhofer regime.

On the other hand, additional interference appears in the far-field zone due to the wavefront structure, resulting in an enlarged image of the grating. As previously noted, the structure of the grating on the sample, T_D, depends on the field structure at distance z_0, as defined by Eq. (2). This dependence leads to variations in the intensity distribution in the far field (see Fig. 7).

It is important to note that shifting the sample along the z-axis alters the spatial spectrum of the grating on the sample, leading to modifications in the diffraction orders. Since Talbot lengths vary for different wavelengths, a dependence on the intensity ratio of the pump and probe beams (p) is also expected.

Fig. 8 | Characterization of FeGd sample. **a** Magneto-optical Kerr-effect (MOKE) measurements in the polar geometry for the FeGd sample and **b** magnetic force microscopy image (right). The white scale bar in (**b**) corresponds to a length of 4 μm.

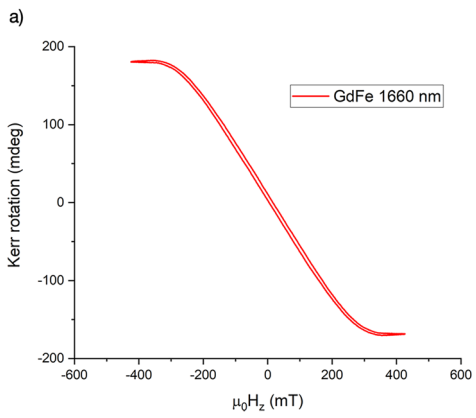

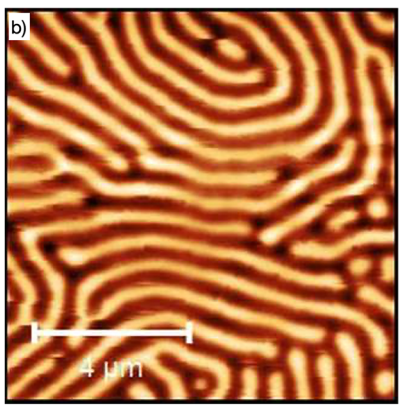

FeGd sample

FeGd films have been deposited by Ar magnetron co-sputtering from two elemental targets of Fe and Gd on a Si_3N_4 membrane. The base pressure of the main chamber was $<2 \times 10^{-8}$ torr and the Ar working pressure was set to 3 mTorr. The thickness of the film was estimated to be about 1.7 μm. The film exhibited a perpendicular magnetic anisotropy with a saturating field of 200 mT determined by magneto-optical Kerr-effect (MOKE) measurements in the polar geometry (Fig. 8a). The magnetic multidomain state at remanence was determined by magnetic force microscopy, as depicted in Fig. 8b. During the TG measurements, the samples were kept inside a uniform magnetic field provided by a permanent magnet perpendicular to the sample surface.

Data availability

Raw data are available upon reasonable and motivated request.

Code availability

Codes employed in the simulations are available upon reasonable and motivated request.

Received: 11 February 2025; Accepted: 5 June 2025;
Published online: 18 June 2025

References

1. Bloembergen, N. Nonlinear optics and spectroscopy. *Rev. Mod. Phys.* **54**, 685–695 (1982).
2. Chergui, M., Beye, M., Mukamel, S., Svetina, C. & Masciovecchio, C. Progress and prospects in nonlinear extreme-ultraviolet and X-ray optics and spectroscopy. *Nat. Rev. Phys.* **5**, 578–596 (2023).
3. Fidler, A. P. et al. Nonlinear XUV signal generation probed by transient grating spectroscopy with attosecond pulses. *Nat. Commun.* **10**, 1384 (2019).
4. Quintero-Bermudez, R., Drescher, L., Eggers, V., Xiong, K. G. & Leone, S. R. Attosecond transient grating spectroscopy with near-infrared grating pulses and an extreme ultraviolet diffracted probe. *ACS Photonics* **12**, 2097–2105 (2025).
5. Cao, W., Warrick, E. R., Fidler, A., Neumark, D. M. & Leone, S. R. Noncollinear wave mixing of attosecond XUV and few-cycle optical laser pulses in gas-phase atoms: toward multidimensional spectroscopy involving XUV excitations. *Phys. Rev. A* **94**, 053846 (2016).
6. Gaynor, J. D. et al. Solid state core-exciton dynamics in NaCl observed by tabletop attosecond four-wave mixing spectroscopy. *Phys. Rev. B* **103**, 245140 (2021).
7. Rupprecht, P., Puskar, N. G., Neumark, D. M. & Leone, S. R. Extracting doubly excited state lifetimes in helium directly in the time domain with attosecond noncollinear four-wave-mixing spectroscopy. *Phys. Rev. Res.* **6**, 043100 (2024).
8. Bencivenga, F. et al. Four-wave mixing experiments with extreme ultraviolet transient gratings. *Nature* **520**, 205–208 (2015).
9. Maznev, A. A. et al. Generation of coherent phonons by coherent extreme ultraviolet radiation in a transient grating experiment. *Appl. Phys. Lett.* **113**, 221905 (2018).
10. Bohinc, R. et al. Nonlinear XUV-optical transient grating spectroscopy at the Si L2,3–edge. *Appl. Phys. Lett.* **114**, 181101 (2019).
11. Svetina, C. et al. Towards X-ray transient grating spectroscopy. *Opt. Lett.* **44**, 574–577 (2019).
12. Rouxel, J. R. et al. Hard X-ray transient grating spectroscopy on bismuth germanate. *Nat. Photonics* **15**, 499–503 (2021).
13. Bencivenga, F. et al. Nanoscale transient gratings excited and probed by extreme ultraviolet femtosecond pulses. *Sci. Adv.* **5**, eaaw5805 (2019).
14. Ksenzov, D. et al. Nanoscale transient magnetization gratings created and probed by femtosecond extreme ultraviolet pulses. *Nano Lett.* **21**, 2905–2911 (2021).
15. Yao, K. et al. All-optical switching on the nanometer scale excited and probed with femtosecond extreme ultraviolet pulses. *Nano Lett.* **22**, 4452–4458 (2022).
16. Morillo-Candas, A. S. et al. Coherent all X-ray four wave mixing at core shell resonances. Preprint at https://doi.org/10.48550/arXiv.2408.11881 (2024).
17. H. Talbot LXXVI. Facts relating to optical science. No. IV. *Lond. Edinb. Dublin Philos. Mag. J. Sci*. https://doi.org/10.1080/14786443608649032 (1836).
18. Ishikawa, T. et al. A compact X-ray free-electron laser emitting in the sub-angstrom region. *Nat. Photonics* **6**, 540–544 (2012).
19. Hara, T. et al. Two-colour hard X-ray free-electron laser with wide tunability. *Nat. Commun.* **4**, 2919 (2013).
20. Kameshima, T. et al. Development of an X-ray pixel detector with multi-port charge-coupled device for X-ray free-electron laser experiments. *Rev. Sci. Instrum.* **85**, 033110 (2014).
21. Roberto, J. B., Batterman, B. W. & Keating, D. T. Diffraction studies of the (222) reflection in Ge and Si: anharmonicity and the bonding electron. *Phys. Rev. B* **9**, 2590–2599 (1974).
22. Eichler, H. J., Günter, P. & Pohl, D. W. Diffraction and four-wave mixing theory. in *Laser-Induced Dynamic Gratings* (eds Eichler, H. J., Günter, P. & Pohl, D. W.) 94–122. https://doi.org/10.1007/978-3-540-39662-8_4 (Springer, 1986).
23. Marroux, H. J. B. et al. Separation of kinetic rate orders in extreme ultraviolet transient grating spectroscopy. *J. Phys. B At. Mol. Opt. Phys*. https://doi.org/10.1088/1361-6455/ad421f (2024).
24. Lu, Z. Q., Quinn, T. & Reehal, H. S. Polarization-dependent Raman spectra of thin crystalline silicon films. *J. Appl. Phys.* **97**, 033512 (2005).
25. Riffe, D. M. & Sabbah, A. J. Coherent excitation of the optic phonon in Si: transiently stimulated Raman scattering with a finite-lifetime electronic excitation. *Phys. Rev. B* **76**, 085207 (2007).
26. Hase, M., Katsuragawa, M., Constantinescu, A. M. & Petek, H. Coherent phonon-induced optical modulation in semiconductors at terahertz frequencies. *N. J. Phys.* **15**, 055018 (2013).
27. Fainozzi, D. et al. Stimulated Brillouin scattering in the time domain at 1 nm−1 wave vector. *Phys. Rev. Lett.* **132**, 033802 (2024).
28. Huang, Y. et al. Nanometer-scale acoustic wave packets generated by stochastic core-level photoionization events. *Phys. Rev. X* **14**, 041010 (2024).
29. Wahlstrand, J. K., Merlin, R., Li, X., Cundiff, S. T. & Martinez, O. E. Impulsive stimulated Raman scattering: comparison between phase-sensitive and spectrally filtered techniques. *Opt. Lett.* **30**, 926 (2005).
30. Chen, Z., Gao, Y., Minch, B. C. & DeCamp, M. F. Coherent optical phonon generation in Bi3Ge4O12. *J. Phys. Condens. Matter* **23**, 385402 (2011).
31. Sabbah, A. J. & Riffe, D. M. Femtosecond pump-probe reflectivity study of silicon carrier dynamics. *Phys. Rev. B* **66**, 165217 (2002).
32. Hase, M., Kitajima, M., Constantinescu, A. M. & Petek, H. The birth of a quasiparticle in silicon observed in time–frequency space. *Nature* **426**, 51–54 (2003).
33. Li, J. J., Chen, J., Reis, D. A., Fahy, S. & Merlin, R. Optical probing of ultrafast electronic decay in Bi and Sb with slow phonons. *Phys. Rev. Lett.* **110**, 047401 (2013).
34. Ohno, M. & van Riessen, G. A. Hole-lifetime width: a comparison between theory and experiment. *J. Electron Spectrosc. Relat. Phenom.* **128**, 1–31 (2003).
35. Son, S.-K., Chapman, H. N. & Santra, R. Multiwavelength anomalous diffraction at high X-ray intensity. *Phys. Rev. Lett.* **107**, 218102 (2011).

36. Miotto, M., Milanetti, E., Mincigrucci, R., Masciovecchio, C. & Ruocco, G. High-throughput interactome determination via sulfur anomalous scattering. *J. Phys. Chem. Lett.* **15**, 3478–3485 (2024).
37. Katayama, K., Sato, K., Sugiya, H. & Shoji, T. Near-field heterodyne transient grating spectroscopy. *Chem. Phys. Lett.* **479**, 306–309 (2009).
38. Salvati Manni, L., Wood, K., Klapproth, A. & Warr, G. G. Inelastic neutron scattering and spectroscopy methods to characterize dynamics in colloidal and soft matter systems. *Adv. Colloid Interface Sci.* **326**, 103135 (2024).
39. Ament, L. J. P., van Veenendaal, M., Devereaux, T. P., Hill, J. P. & van den Brink, J. Resonant inelastic x-ray scattering studies of elementary excitations. *Rev. Mod. Phys.* **83**, 705–767 (2011).
40. Yan, J. et al. Terawatt-attosecond hard X-ray free-electron laser at high repetition rate. *Nat. Photonics* **18**, 1293–1298 (2024).
41. Tono, K. et al. Beamline, experimental stations and photon beam diagnostics for the hard x-ray free electron laser of SACLA. *N. J. Phys.* **15**, 083035 (2013).
42. Yumoto, H. et al. Focusing of X-ray free-electron laser pulses with reflective optics. *Nat. Photonics* **7**, 43–47 (2013).
43. Tamasaku, K. et al. Inline spectrometer for shot-by-shot determination of pulse energies of a two-color X-ray free-electron laser. *J. Synchrotron Radiat.* **23**, 331–333 (2016).
44. Gorelick, S., Guzenko, V. A., Vila-Comamala, J. & David, C. Direct e-beam writing of dense and high aspect ratio nanostructures in thick layers of PMMA for electroplating. *Nanotechnology* **21**, 295303 (2010).
45. Goloborodko, A. Wavefront curvature restoration by a sensor based on the Talbot phenomenon under Gaussian illumination. *J. Opt. Soc. Am. A* **40**, B8–B14 (2023).

Acknowledgements

This work was supported by the "Severo Ochoa" Programme for Centres of Excellence in R&D (CEX2020-001039S/AEI/10.13039/501100011033) and Spanish Ministry of Science, Innovation, and Universities through project PID2023-152154NB-C21, the National Centre of Competence in Research (NCCR): Molecular Ultrafast Science and Technology (MUST, grant 51NF40-183615) of the Swiss National Science Foundation, the European Research Council (ERC) Advanced Grant DYNAMOX (no. 695197) and the COST Action CA22148 NEXT. H.U. acknowledges support of the European Union's Horizon 2020 Research and Innovation program (Marie Skłodowska-Curie Grant 801459–FP-RESOMUS). R.C. acknowledges the Italian Ministry of Foreign Affairs and International Cooperation (MAECI), Grant no. PGR12320 - U-DYNAMEC - CUP B53C23006060001. J.R.R. was supported by the U.S. Department of Energy (DOE), Office of Science, Basic Energy Science (BES), Chemical Sciences, Geosciences and Biosciences Division, under Contract No. DE-AC02-06CH11357. M.C. acknowledges support of the ERC Advanced Grant CHIRAX (no. 101095012). R.C. and P.C. acknowledge the Nanoscience Foundry and Fine Analysis (NFFA-MUR Italy Progetti Internazionali) facility. C.S. acknowledges the Material Science beamline at Swiss Light Source—PSI for support in the characterization of the phase masks and samples. We thank Dr A. Maznev, Prof. K.A. Nelson and Prof. D.A. Reis for useful and stimulating discussions.

Author contributions

C.S. conceived, designed and coordinated the project. U.S. proposed the diffraction detection geometry. T.O., I.I., Y.I., K.T., M.Y., J.Y. realized the experimental setup at SACLA. H.U. and K.Y. performed the experiment on-site while U.S., S.G., J.R.R., F.B., R.M., J.V.C., E.F., B.R., D.F., L.M.D.L., P.C., M.B., R.C., and C.S. supported remotely. J.V.C. and C.D. manufactured the phase mask and H.U., C.D., J.V.C., B.R., L.M.D.L., E.P., S.G., M.C.A.Z., B.P., and C.S. performed its characterization at the Material Science beamline at Swiss Light Source. V.S. and A.H. produced and characterized the FeGd thin film. E.F. reduced the raw data and performed the data analysis with the help of D.F. and C.S.; C.Se. and A.G. developed the code to perform the wave-front propagation simulations. A.Ge. made the 3D models of the experiment and manufactured the sample and phase-masks holders. D.F. realized the figures of the reported traces. M.C., M.Be., C.M., U.S., E.F., H.U., J.R.R., C.Se., A.G., D.F. and C.S. wrote the manuscript with contributions from all authors.

Funding

Open Access funding enabled and organized by Projekt DEAL.

Competing interests

The authors declare no competing interests.

Additional information

Supplementary information The online version contains supplementary material available at https://doi.org/10.1038/s42005-025-02178-y.

Correspondence and requests for materials should be addressed to Eugenio Ferrari, Hiroki Ueda or Cristian Svetina.

Peer review information *Communications Physics* thanks the anonymous reviewers for their contribution to the peer review of this work. A peer review file is available.

[1]Deutsches Elektronen-Synchrotron DESY, Hamburg, Germany. [2]PSI Center for Accelerator Science and Engineering, Villigen, Switzerland. [3]PSI Center for Photon Science, Villigen, Switzerland. [4]Institute of Applied physics, University of Bern, Bern, Switzerland. [5]RIKEN SPring-8 Center, Sayo-gun, Hyogo, Japan. [6]Elettra Sincrotrone Trieste S.C.p.A., Trieste, Italy. [7]DECTRIS Ltd, Baden-Daettwil, Switzerland. [8]Dipartimento di Fisica, Università degli Studi di Milano, Milano, Italy. [9]CNR - Istituto Officina dei Materiali (IOM), Unità di Trieste, Basovizza, TS, Italy. [10]PWGP Labs, Bucha, Kyiv Region, Ukraine. [11]PSI Center for Neutron and Muon Sciences, Villigen, Switzerland. [12]Laboratory for Mesoscopic Systems, Department of Materials, ETH Zurich, Zurich, Switzerland. [13]Japan Synchrotron Radiation Research Institute, Sayo-gun, Hyogo, Japan. [14]Chemical Sciences and Engineering Division, Argonne National Laboratory, Lemont, IL, USA. [15]Department of Physics, Polytechnic University of Catalonia, Terrassa (Barcelona), Spain. [16]Research Center for Precision Engineering, Graduate School of Engineering, Osaka University,

Osaka, Japan. [17]Institute for Molecular Science, Okazaki, Aichi, Japan. [18]NanoTerasu center, National Institutes for Quantum Science and Technology, Sendai, Miyagi, Japan. [19]Fysikum, Stockholm University, Stockholm, Sweden. [20]Lausanne Centre for Ultrafast Science (LACUS), ISIC, Ecole Polytechnique Fédérale de Lausanne, Lausanne, Switzerland. [21]Madrid Institute for Advanced Studies, IMDEA Nanociencia, Calle Faraday 9, Ciudad Universitaria de Cantoblanco, Madrid, Spain. [22]European XFEL, Schenefeld, Germany. [23]These authors contributed equally: Eugenio Ferrari, Hiroki Ueda.
✉e-mail: eugenio.ferrari@desy.de; hiroki.ueda@psi.ch; cristian.svetina@imdea.org